

Article

Experimental Study on the Thermal Reduction of CO₂ by Activated Solid Carbon-Based Fuels

Siyuan Zhang ^{1,2} , Chen Liang ¹, Zhiping Zhu ^{1,2,*} and Ruifang Cui ^{1,2}

¹ State Key Laboratory of Coal Conversion, Institute of Engineering Thermophysics, Chinese Academy of Sciences, Beijing 100190, China; zhangsiyuan@iet.cn (S.Z.); liangchen@iet.cn (C.L.); cuiruifang@iet.cn (R.C.)

² University of Chinese Academy of Sciences, Beijing 100049, China

* Correspondence: zhuzhiping@iet.cn

Abstract: For achieving CO₂ thermal reduction, a technology combining solid carbon activation and high-temperature CO₂ reduction was proposed, named as activated-reduction technology. In this study, this technology is realized by using a circulating fluidized bed and downdraft reactor. Reduced agent parameters (O₂/C and CO₂ concentration) greatly affect the reduction effect of CO₂. In addition, the effect of the activation process on different carbon-based materials can help to broaden the range of carbon-based materials used for CO₂ reduction, which is also an important issue. The following three points have been studied through experiments: (1) the influence of the characteristics of the reduced agent (CO₂ concentration and O₂/C) on CO₂ reduction; (2) the performance of different chars in CO₂ reduction; and (3) the activation effect of solid carbon. The activation process can develop the pore structure of coal gasification char and transform it into activated char with higher reactivity. The CO concentration in the tail gas is a crucial factor limiting the effectiveness of CO₂ reduction, with an experimentally determined upper limit of around 55% at 1200 °C. If CO concentration is far from the upper limit, temperature becomes the significant influencing factor. When the reduced agent O₂/C is 0.18, the highest net CO₂ reduction of 0.021 Nm³/kg is achieved at 60% CO₂ concentration. When the reduced agent CO₂ concentration is 50%, the highest net CO₂ reduction of 0.065 Nm³/kg is achieved at 0.22 O₂/C. Compared with CPGC, YHGC has higher reactivity and is more suitable for CO₂ reduction. The activation process helps to reduce the differences between raw materials.

Keywords: activated-reduction technology; CO₂ utilization; char; gasification



Citation: Zhang, S.; Liang, C.; Zhu, Z.; Cui, R. Experimental Study on the Thermal Reduction of CO₂ by Activated Solid Carbon-Based Fuels. *Energies* **2024**, *17*, 2164. <https://doi.org/10.3390/en17092164>

Academic Editor: Albert Ratner

Received: 28 March 2024

Revised: 17 April 2024

Accepted: 30 April 2024

Published: 1 May 2024



Copyright: © 2024 by the authors. Licensee MDPI, Basel, Switzerland. This article is an open access article distributed under the terms and conditions of the Creative Commons Attribution (CC BY) license (<https://creativecommons.org/licenses/by/4.0/>).

1. Introduction

Climate change is a great challenge that humanity will face in the foreseeable future [1]. As one of the major greenhouse gases, the reduction of CO₂ is of high interest to the global community [2]. The utilization of CO₂ can not only help achieve carbon reduction, but also convert CO₂ into value-added products [3]. At present, the research results of the technical ways of carbon dioxide utilization are mainly in the field of catalytic utilization, such as catalytic, electrocatalytic, photo-catalytic types, and so on [4]. In addition, the reduction of CO₂ by carbon-based materials at high temperatures is also a promising approach [5,6]. This process primarily relies on the Boudouard reaction, as illustrated in R1 [7].



This method can be integrated with the existing large-scale coal gasification industry, facilitating the rapid realization of the large-scale utilization of CO₂ [8]. CO is the reduction product of CO₂. Together with green hydrogen, they can be used by the subsequent synthesis gas unit of the existing gasification facility for chemical synthesis [3].

The chemical properties of CO₂ are relatively stable. CO₂ obviously undergoes the Boudouard reaction with low-quantivalence carbon only at high temperatures [9]. The physicochemical properties of char also play a crucial role in the reduction of CO₂. Based on

this, activated-reduction technology has been developed. This technology combines solid carbon activation with high-temperature CO₂ reduction. Solid carbon is first activated in the activation unit and then reduces CO₂ at a high temperature (>1100 °C) in the reduction unit. The CO₂ reduction through activated reduction technology does not require the addition of catalysts, and there is no problem with product selectivity, so this technology is cost-effective.

The rate of the Boudouard reaction is significantly affected by the magnitude and accessibility of the surface area of chars [10]. Vamvuka et al. [11] investigated the reactivity of municipal solid waste, sewage sludge, and waste paper. Among them, waste paper exhibited the highest reactivity, with the largest surface area among these materials. Duman et al. [12] observed that the char with a higher surface area was found to be more reactive than char with a lower surface area. However, Tong et al. [13] investigated the reactivity of biomass char obtained at different pyrolysis temperatures. They have indicated that, in comparison to surface area, the impact of the active site is more significant on reactivity. The active sites or carbon structure in char is commonly characterized using Raman spectra [14–16]. Guizani et al. [17] observed the relationship between carbon structure and the reactivity of char and found that the reactivity index (R_{index}) has a good linear relationship with I_V/I_D . They thought that the more reactive and amorphous small aromatic structures that char obtains, compared to condensed structures, the higher its reactivity. Zhang et al. [18] employed Raman to examine the carbon structure of char. Through analyzing the relationship between gasification reactivity and physicochemical properties, they suggested that carbon structure plays a crucial role in gasification reactivity.

During the gasification process in the circulating fluidized bed (CFB), the specific surface area of the raw material increases, and the concentration of stable graphite structure decreases [19–21]. In this study, a CFB was used as the activation unit, which enhances the reactivity of carbon-based materials and preheats carbon-based materials and gases [14,22]. The downdraft reactor (DR) was used as the reduction unit, providing a high-temperature zone for the occurrence of the Boudouard reaction.

In addition to the physicochemical properties of solid carbon, temperature and CO₂ partial pressure significantly affect the Boudouard reaction. Temperature is the most critical parameter influencing the Boudouard reaction [3,23]. Increasing the reaction temperature promotes the Boudouard reaction [24–26]. Liu et al. [27] used thermal balance to investigate the effect of temperature on the CO₂ gasification of three types of char. The results showed that as the temperature increased from 1000 °C to 1300 °C, the reactivity of all the chars significantly increased. Jing et al. [28] studied the CO₂ gasification characteristics of fine chars in the temperature range of 1000–1300 °C. Their results showed that it took 36 min for fine chars to achieve 90% carbon conversion at 1000 °C, whereas only 2 min was required at 1300 °C. Xie et al. [29] investigated the Boudouard reaction rate of biochar at different temperatures and observed that, with rising temperature, their gasification rates increased significantly. The maximum reaction rate increased by 4.4 times from 750 °C to 850 °C.

However, these studies were conducted using thermogravimetric analysis (TGA) or tube furnaces. These experimental furnaces can all be fully heated by external sources. However, the actual industrial process is typically self-sustained. In the actual industrial process, the high temperatures required for CO₂ reduction are typically derived from the combustion of solid carbon. Therefore, there exists a competitive relationship in the actual industrial process: while high temperatures can facilitate the reduction of CO₂, the cost of these high temperatures comes from the generation of CO₂. Liang et al. [30] conducted O₂/CO₂ gasification experiments by using a bench-scale self-sustained CFB. They found that when the O₂/C molar ratio increased from 0.39 to 0.64, the maximum temperature of the CFB rose from approximately 892 °C to about 938 °C. However, the CO₂ yield increased from 2.22 Nm³/kg to 3.57 Nm³/kg. This indicates that, due to the influence of combustion reactions, for self-sustained systems, increasing the temperature may potentially weaken the reduction effectiveness of CO₂.

The partial pressure of CO₂ also affects the Boudouard reaction, with higher CO₂ partial pressures generally being more favorable for the reaction. Feroso et al. [31] used biomass char as the raw material and examined the impact of CO₂ partial pressure on the reaction rate using TGA. The results showed that the Boudouard reaction rate increased with the increase in CO₂ partial pressure. Malekshahian et al. [32] observed a similar trend when using petroleum coke as a raw material, with the gasification rate increasing more than fourfold as the CO₂ pressure was raised from 0.1 MPa to 2.4 MPa. Considering that CO₂ is a reactant, its increased partial pressure can enhance the Boudouard reaction by increasing the adsorption of CO₂ on active sites [33,34]. However, when the CO₂ concentration is high, further increasing the CO₂ concentration may not significantly promote the reaction. Ahmed et al. [35] noted that for woodchip char, when the total pressure was 2 bar and the CO₂ partial pressure was reduced from 1.5 bar to 1.2 bar, the change in CO₂ partial pressure had little effect on the Boudouard reaction rate. Irfan et al. [36] further processed and analyzed the CO₂ gasification experimental results of New Zealand coal char by Kajitani et al. [37] using a pressurized drop tube furnace. It was observed that as the CO₂ concentration increased from 8% to 25%, the Boudouard reaction rate changed significantly with the CO₂ concentration, but the impact of further increasing the CO₂ concentration on the Boudouard reaction rate was minimal.

The research results above indicate that an increase in CO₂ concentration is beneficial to the Boudouard reaction to a certain extent. However, in actual processes, similar to the effect of temperature, there is a competitive mechanism that influences the intensity of the Boudouard reaction when increasing CO₂ concentration. An increase in CO₂ concentration implies an increase in the amount of CO₂ being supplied. This leads to an increase in the sensible heat required to heat the CO₂, which may result in a decrease in temperature. At this point, the strengthening effect of increased CO₂ concentration on the Boudouard reaction coexists with the inhibitory effect of temperature reduction on the reaction. It is challenging to directly determine the impact of CO₂ concentration on CO₂ reduction within a self-sustained system.

Integrating the research findings above, the current technological approach of reducing CO₂ through activation-reduction technology is facing the following issues: (1) the impact of temperature on CO₂ reduction within self-sustained systems; (2) the influence of CO₂ concentration on CO₂ reduction within self-sustained systems; and (3) the selection of suitable carbon-based raw materials for CO₂ reduction and the effects of the activation process on these materials. This study employs two types of char as raw materials for CO₂ reduction experiments on an activated-reduction bench-scale platform. The effectiveness of the activation process in a CFB and the impact of CO₂ concentration and O₂/C in the agent injected into a DR on CO₂ reduction are investigated. The CO₂ reduction effects of the two types of char are also compared. This work aims to provide a solution that simultaneously utilizes char and CO₂, offering theoretical and data references for subsequent industrial practices.

2. Experimental

2.1. Test Rig and Experimental Process

The CO₂ reduction experiments were conducted in an activated-reduction bench-scale self-sustained platform, of which a schematic diagram is presented in Figure 1. The activated-reduction bench-scale platform is shown in Figure 2. The test rig has two main units: the activation unit (CFB, including a riser, cyclone, and seal loop) and the reduction unit (DR). Except for these two main units, the platform includes a series of auxiliary equipment, including the air supply system (providing air, O₂, CO₂, steam, and N₂), the cleaning system (with a gas cooler, water pump, water tank, and bag filter) and the auxiliary heating system (including electric heating systems of the CFB and DR, and the gas heater). There are three main temperature measurement points, namely T1, T9, and T10 (shown in Figure 1). T1 measures the temperature at the bottom of the riser, T9 measures the

temperature at the top of the DR (40 mm below the top), and T10 measures the temperature in the middle of the DR (235 mm below the top).

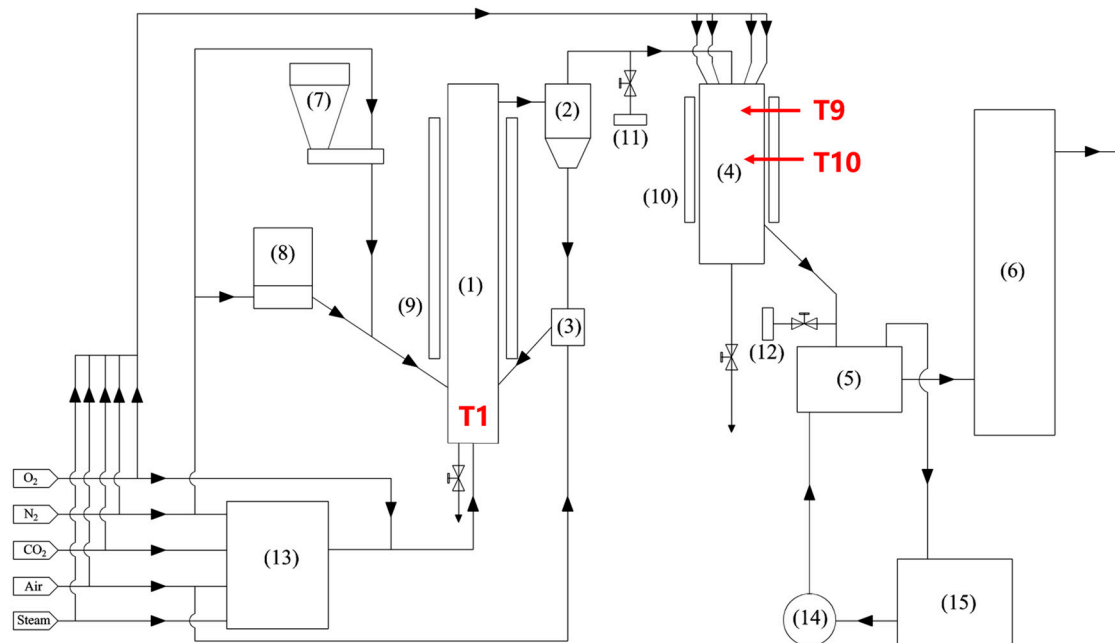


Figure 1. Schematic diagram of the activated-reduction bench-scale platform: (1) riser, (2) cyclone, (3) loop seal, (4) downdraft reactor, (5) gas cooler, (6) bag filter, (7) feeder, (8) pneumatic conveying equipment, (9) electric furnace of the CFB, (10) electric furnace of the DR, (11) sampling port I, (12), sampling port II, (13) gas heater, (14) water pump, (15) water tank.



Figure 2. Activated-reduction bench-scale platform.

When the experiment was formally initiated, only O_2 , CO_2 , and a small amount of N_2 were introduced into the system. N_2 served as the conveying gas to transport char into the system. O_2 and CO_2 , entering the CFB are designated as the active agent. O_2 and CO_2 directly entering the DR are designated as the reduced agent. The gas departing from the CFB is termed the activation unit gas, and the gas departing from the DR is termed the reduction unit gas. The solid separated from the activation unit gas is identified as activated char.

Before commencing the experiment, 25 kg of quartz sand was introduced into the CFB as the bed material. The particle size distribution of quartz sand is illustrated in Figure 3.

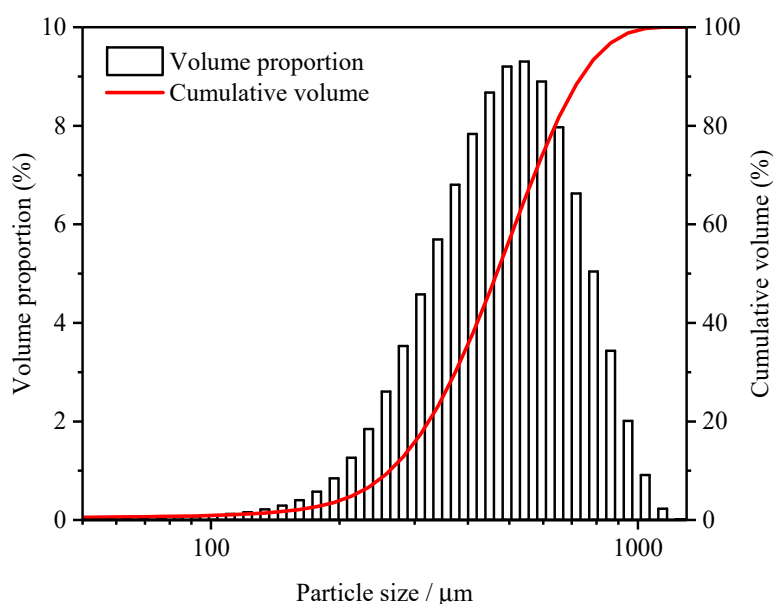


Figure 3. The particle size distribution of quartz sand.

The electric furnace and gas heater were activated initially. Once T1 reached 600 °C, the pneumatic conveying equipment was initiated, and the air flow was increased. The CFB warmed up in the combustion state. When T1 rose to 800 °C, T1 remained basically unchanged by adjusting the feed rate and air flow. The experiment waited for T9 to reach 800 °C. After reaching the required temperature, CO₂ and O₂ were successively introduced, and air flow was stopped. The feed rate was increased to transform the CFB into the gasification state. Once stabilized, the reduced agent was introduced to raise T9 in the combustion state. When T9 reached 1100 °C, the active agent and the reduced agent, as well as the feed rate, were adjusted to meet the conditions required for the operation. The temperature variation did not exceed 20 °C, signifying the commencement of the operation, and each operation was sustained for 1 h. The electric furnace and gas preheating temperature remained constant throughout the experiments. The electric furnace of the CFB and DR were maintained at 14.8 kW and 8.3 kW, respectively. The gas preheating temperature was set at 300 °C.

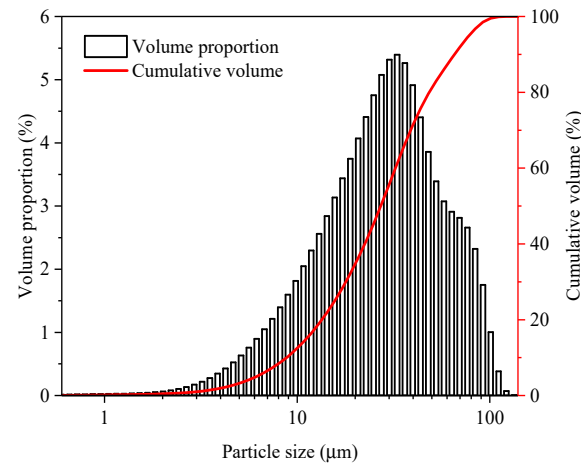
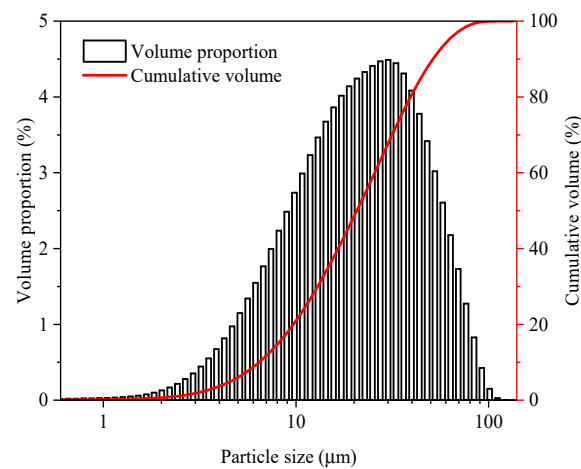
2.2. Material Conditions

In this study, two kinds of coal gasification chars, YHGC (Yihua gasification char) and CPGC (Chiping gasification char), were used as raw materials for reducing CO₂. YHGC is derived from the solid phase outlet of the cyclone separator of the 720 t/d atmospheric CFB gasification plant in Xinjiang. CPGC is derived from the solid phase outlet of the cyclone separator of the 40,000 m³/h atmospheric CFB gasification plant in Shandong. The proximate and ultimate analyses of YHGC and CPGC are presented in Table 1, where M represents moisture, FC represents fixed carbon, V represents volatiles, A represents ash, C represents carbon element, H represents hydrogen element, O represents oxygen element, N represents nitrogen element, S represents sulfur element, and Q_{net,ad} represents the net calorific value on the air-dry basis. The particle size analysis of YHGC and CPGC are shown in Figures 4 and 5, respectively. The particle diameters corresponding to the cumulative volume fractions of 10% (d_{10}), 50% (d_{50}), and 90% (d_{90}) of YHGC are 9.67, 29.82, and 72.06 μm, respectively. The d_{10} , d_{50} , and d_{90} of CPGC are 7.06, 22.72, and 56.43 μm, respectively. It can be observed that the particle size ranges of YHGC and CPGC are approximately consistent, mostly below 100 μm. In comparison to CPGC, the particle size distribution of YHGC is more concentrated.

Table 1. Proximate and ultimate analyses of YHGC and CPGC.

Material	Proximate Analyze/wt%					Ultimate Analyze/wt%				$Q_{net,ad}$ MJ/kg
	M_{ad}	FC_{ad}	V_{ad}	A_{ad}	C_{ad}	H_{ad}	O_{ad}	N_{ad}	S_{ad}	
YHGC	1.08	64.05	7.08	27.79	66.83	0.56	3.32	0.24	0.18	22.94
CPGC	6.12	77.18	2.04	14.65	74.86	0.73	2.57	0.62	0.34	28.85

Note: ad represents the air-dry basis.

**Figure 4.** The particle size distribution of YHGC.**Figure 5.** The particle size distribution of CPGC.

2.3. Calculation and Analysis Methods

The measurement of gas samples was conducted using the Agilent 490 GC (Agilent Technologies Inc., Santa Clara, CA, USA). Assuming no reactions occur with N_2 in the activated-reduction system, calculations were performed using nitrogen balance [30,38]. Although O_2 and CO_2 are the primary gases used in this study, N_2 was utilized as the conveying gas for the transport of carbon-based materials. Consequently, there was a presence of N_2 in the system. (1) and (2) were used to calculate the net yields of component i in the activation unit ($y_{i,CFB}$) and the reduction unit ($y_{i,DR}$), respectively [39].

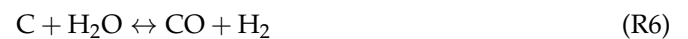
$$y_{i,CFB} = x_{i,CFB} \cdot \frac{y_{N_2,inCFB}}{x_{N_2,CFB}} - y_{i,inCFB} \quad (1)$$

$$y_{i,DR} = x_{i,DR} \cdot \frac{y_{N_2,inCFB}}{x_{N_2,DR}} - y_{i,inDR} \quad (2)$$

where $x_{i,CFB}$ is the concentration of component i in the activation unit gas, $y_{i,inCFB}$ is the flow rate of component i entering the activation unit, corresponding to per mass of raw materials (Nm^3/kg), $x_{i,DR}$ is the concentration of component i in the reduction unit gas, and $y_{i,inDR}$ is the flow rate of component i entering the reduction unit, corresponding to per mass of raw materials (Nm^3/kg). The component i includes H_2 , CO , CO_2 , O_2 and N_2 .

$y_{\text{CO}_2,DR}$ may be a negative value, signifying that the CO_2 leaving the reduction unit is less than the CO_2 supplied to the reduction unit. In this case, a net conversion of CO_2 is achieved.

Except for the Boudouard reaction, the main reactions occurring in the activated-reduction system are listed below [30]. Among these reactions, R2 to R5 are the main combustion reactions. R6 is the steam char gasification reaction, and R7 is the water gas shift reaction (WGSR).



In order to better understand the reactions occurring in the reduction unit, calculations were performed using $y_{i,DR}$. Considering that CH_4 is not involved in the experimental results, it is assumed that three main reactions, R1, R3, and R6 occur in the reduction unit, and the changes in CO , CO_2 , and H_2 are determined by these three reactions. This assumption, based on experimental results, packages together the possible reactions occurring in the reduction unit. For example, the generation path of CO_2 , besides R3, also includes $\text{R2} + \text{R4}$. However, considering the large gap between particles in the descending bed, the combustion model of single film or double film was used to describe the combustion of particles. At this time, $\text{R2} + \text{R4}$ is completed in the boundary layer of the particle, and the combustion process of carbon can be described by R3 as observed from the main stream region. In addition to R1, there are also R7 reactions associated with CO_2 reduction. However, the hydrogen content in the system in this study is small, and the reduction of CO_2 mainly relies on R1. Therefore, R1 is used to describe the reduction process of CO_2 . The same simplification applies to H_2 . Therefore, $y_{\text{R1},DR}$, $y_{\text{R3},DR}$, and $y_{\text{R6},DR}$ (corresponding to the occurrence of $\text{C} + \text{CO}_2 \rightarrow 2\text{CO}$, $\text{C} + \text{O}_2 \rightarrow \text{CO}_2$, and $\text{C} + \text{H}_2\text{O} \rightarrow \text{CO} + \text{H}_2$ in the reduction unit, mol/kg) can be calculated according to the following equations:

$$y_{\text{R1},DR} = y_{\text{R3},DR} - \frac{y_{\text{CO}_2,DR} \text{ kmol}}{22.4 \text{ Nm}^3} \cdot 1000 \frac{\text{mol}}{\text{kmol}} \quad (3)$$

$$y_{\text{R3},DR} = -\frac{y_{\text{O}_2,DR} \text{ kmol}}{22.4 \text{ Nm}^3} \cdot 1000 \frac{\text{mol}}{\text{kmol}} \quad (4)$$

$$y_{\text{R6},DR} = \frac{y_{\text{H}_2,DR} \text{ kmol}}{22.4 \text{ Nm}^3} \cdot 1000 \frac{\text{mol}}{\text{kmol}} \quad (5)$$

The analysis of raw materials and the activated chars primarily involved pore structure analysis and Raman analysis. N_2 was used as the adsorption medium for the pore analysis. The BET method was employed to calculate the specific surface area [40], while the BJH method was used for pore volume calculation [41]. The Raman spectra results were subjected to peak fitting, dividing them into five peaks. Refer to Table 2 for specific details.

Table 2. Raman peak assignment [19,42–44].

Peak Name	Functional Groups	Position	Type
D ₄	Hybrid bonds of sp ² and sp ³	1150 cm ⁻¹	Lorentzian peak
D ₁	In-plane defects; Edge effects	1350 cm ⁻¹	Lorentzian peak
D ₃	Amorphous sp ² hybrid bonds	1530 cm ⁻¹	Gaussian peak
G	Graphite structure	1580 cm ⁻¹	Lorentzian peak
D ₂	Intercalate concentration	1620 cm ⁻¹	Lorentzian peak

The peak area ratio is used to describe carbon structures. I_G/I_{all} is employed to characterize the graphitization degree and carbon structure stability [45]. D₃ and D₄ are considered to be associated with reactive sites, and I_{D3+D4}/I_G is used to characterize the disorder degree of carbon structures [19,46].

TGA procedure is outlined as follows:

- (1) Load approximately 15 mg of sample into the TGA apparatus;
- (2) After loading the sample, purge with N₂ for 30 min to remove other gases from the sample chamber;
- (3) Ramp the temperature to 1200 °C at a rate of 20 °C/min while maintaining N₂ flow.
- (4) Upon reaching 1200 °C, hold for 10 min; then, introduce CO₂;
- (5) When the sample weight stabilizes, indicating the completion of the gasification process, initiate the cooling procedure.

The carbon conversion x and reactivity index $R_{0.5}$ are calculated using the (6) [47] and (7) [48], respectively.

$$x = \frac{m_0 - m_t}{m_0 - m_{ash}} \times 100\% \quad (6)$$

$$R_{0.5} = \frac{0.5}{t_{0.5}} \quad (7)$$

where m_0 is the initial mass of char, m_t is the char mass at time t , m_{ash} is the mass after gasification has been completed, and $t_{0.5}$ is the time required for x to reach 50%.

3. Results and Discussion

3.1. Effect of CO₂ Concentration in the Reduced Agent

In the case of the self-sustained system, under the condition of approximately constant O₂/C, variations in CO₂ concentration will impact the temperature and component concentrations of the system, thereby altering the reduction of CO₂. The experimental conditions for different CO₂ concentrations in the reduced agent are outlined in Table 3. Throughout these experimental conditions, while keeping the remaining input conditions constant, only the CO₂ concentration in the reduced agent was adjusted to achieve changes in the operating conditions. Temperature, treated as the dependent variable, was not intentionally controlled.

Table 3. Experimental conditions for different CO₂ concentrations in the reduced agent.

No.	Material	Feed Rate (kg/h)	Active Agent		Reduced Agent	
			Composition	O ₂ /C (Mol/Mol)	Composition	O ₂ /C (Mol/Mol)
1	YHGC	23	O ₂ /CO ₂ (40%/60%)	0.073	O ₂ /CO ₂ (70%/30%)	0.18
2					O ₂ /CO ₂ (60%/40%)	
3					O ₂ /CO ₂ (50%/50%)	
4					O ₂ /CO ₂ (40%/60%)	
5					O ₂ /CO ₂ (30%/70%)	

The temperature profile in the activation unit and the reduction unit under different CO₂ concentrations in the reduced agent is illustrated in Figure 6. It can be observed that

T1 remains approximately constant among different experimental conditions, indicating stable operation. As the CO₂ concentration in the reduced agent increases, T9 and T10 gradually decrease. This is attributed to the increasing demand for CO₂ input, which leads to a gradual rise in the physical sensible heat required to heat CO₂. Compared to T10, T9 changes more. It indicates a more pronounced impact of the variation in CO₂ concentration in the reduced agent on T9. This is mainly because the inlet of the reduced agent is located at the top of the reduction unit. With the increase in CO₂ concentration, it not only affects the temperature by absorbing heat but also decreases the combustion reaction rate. This makes the combustion reaction zone in the reduction unit shift downward. Ultimately, when the CO₂ concentration in the reduced agent reaches 70%, T10 exceeds T9. In addition, the increase in CO₂ concentration also raises the input of the reduced agent. Correspondingly, the increased flow rate of gases in the reduction unit promotes heat transfer, reducing temperature differences at various point.

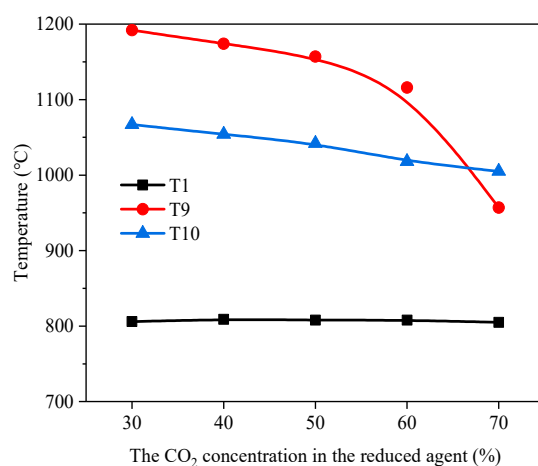


Figure 6. The temperature profiles under different CO₂ concentrations in the reduced agent.

The composition of the activation unit gas and component yields in the activation unit are illustrated in Figure 7. As CH₄ was not detected in any of the experiments in this study, it is not displayed or discussed. The net yields of CO and CO₂ are close, but their concentrations differ significantly. This is mainly attributed to the fact that CO₂ is introduced into the activation unit as part of the active agent.

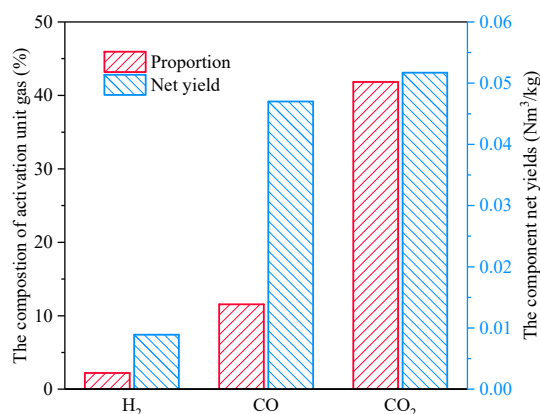


Figure 7. The situation of the activation unit gas under different CO₂ concentrations in the reduced agent.

The situation of reactions in the reduction unit under different CO₂ concentrations in the reduced agent is illustrated in Figure 8. Due to the constant value of O₂/C in the reduced agent, the intensity of combustion reactions remains consistent.

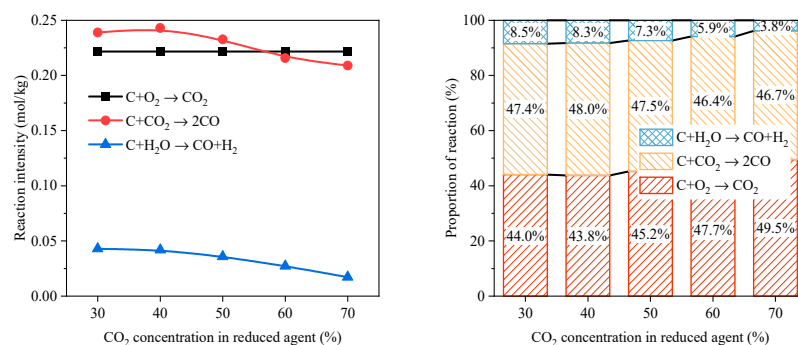


Figure 8. The situation of reactions under different CO₂ concentrations in the reduced agent.

With the increase in CO₂ concentration in the reduced agent, the Boudouard reaction intensity in the reduction unit first increases and then decreases. The Boudouard reaction is promoted by increasing CO₂ concentration in the reduced agent from 30% to 40%. The Boudouard reaction reaches the maximum intensity (0.24 mol/kg) when CO₂ concentration in the reduced agent is 40%. The Boudouard reaction decreases when CO₂ concentration in the reduced agent increases from 40% to 70%. An increase in CO₂ concentration in the reduced agent promotes a decrease in the temperature in the reduction unit (shown in Figure 6), thus weakening the Boudouard reaction. In this series of conditions, the controlling factors of the Boudouard reaction have changed. When CO₂ concentration in the reduced agent is low (<40%), CO₂ concentration has a more significant effect on the Boudouard reaction. While CO₂ concentration in the reduced agent is high (>40%), temperature has a more significant effect. Compared with the change in the Boudouard reaction intensity, the change in the steam char gasification reaction intensity is simple. As CO₂ concentration in the reduced agent increases, the temperature decreases, and the hydrogen-containing component (mainly steam) is diluted. The intensity of the steam char gasification reaction continues to decrease. The trend of the proportion of the reaction is similar with that of the intensity. When CO₂ concentration in the reduced agent is 40%, the proportion of the Boudouard reaction reaches the maximum (48.0%). And the proportion of the steam char gasification reaction continues to decline with the weakening of its intensity.

The composition of the reduction unit gas and component net yields in the reduction unit under different CO₂ concentrations in the reduced agent are illustrated in Figure 9. Because the system is self-sustained, the heat required for the Boudouard reaction comes from the combustion reaction. There are both CO₂ generation and CO₂ reduction present in the reduction unit. Accordingly, in this series of these experimental conditions, there are two cases of positive and negative for net CO₂ yield. When CO₂ concentrations in the reduced agent is less than 50%, the net yield of CO₂ in the reduction unit is negative. This means that the net reduction of CO₂ is achieved in the reduction unit. It can be observed that the net yield of CO and CO₂ in the reduction unit is basically consistent with the trend of changes in the intensity of the Boudouard reaction. This shows that this reaction calculation method can accurately describe the reaction situation in the reduction unit. It can be observed that with the decrease in CO₂ concentration in the reduced agent, the CO proportion of the reduction unit gas gradually increases, but the curve slope gradually decreases. One possible reason is that there is an upper limit for CO concentration. At this time, CO inhibited the Boudouard reaction by occupying the active site [49,50]. This explains why, at low CO₂ concentrations, the temperature is no longer a limiting factor for the Boudouard reaction. At this time, CO concentration is the key factor limiting the Boudouard reaction. The results show that the upper limit of CO concentration is about 55% at 1200 °C. Since the intensity of the Boudouard reaction is the highest when the reducing agent is 40%, the corresponding reduction effect of CO₂ is the best.

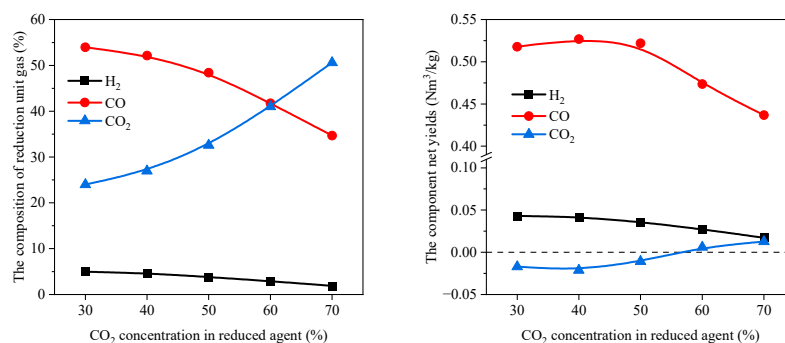


Figure 9. The situation of the reduction unit gas under different CO₂ concentrations in the reduced agent.

The increase in CO₂ concentration in the reduced agent has a promoting effect on CO₂ reduction, which is only effective when CO approaches the upper limit. The increase in CO₂ concentration reduces the CO concentration and weakens the inhibition effect of CO on The Boudouard reaction. When CO concentration is low, reducing CO₂ concentrations in the reduced agent can increase the temperature and effectively increase the net reduction of CO₂. This series of experimental conditions shows that when the reduced agent O₂/C is 0.18 and the temperature of the reduction unit is between 1000 and 1200 °C, the best CO₂ concentrations in the reduced agent for CO₂ reduction is 40%, and the maximum net reduction of CO₂ is 0.021 Nm³/kg.

3.2. Effect of O₂/C in the Reduced Agent

An increase in O₂/C enhances the combustion reaction. Consequently, the corresponding production of CO₂ from combustion reaction increases, which has a negative impact on the overall reduction of CO₂ in the system. However, the increase in the combustion reaction enhances the Boudouard reaction by elevating the temperature, thereby improving CO₂ reduction. Therefore, the variation in O₂/C simultaneously has two opposing effects on the CO₂ reduction. The experimental conditions for different O₂/C in the reduced agent are outlined in Table 4. While keeping the remaining input conditions constant, only the O₂/C in the reduced agent was adjusted to achieve changes in the operating conditions. Temperature, treated as the dependent variable, was not intentionally controlled.

Table 4. Experimental conditions for different O₂/C in the reduced agent.

No.	Material	Feed Rate (kg/h)	The Active Agent		The Reduced Agent	
			Composition	O ₂ /C (Mol/Mol)	Composition	O ₂ /C (Mol/Mol)
6	YHGC	23	O ₂ /CO ₂ (50%/50%)	0.11	O ₂ /CO ₂ (50%/50%)	0.12
7						0.17
8						0.22
9						0.27

The temperature profile in the activation unit and the reduction unit under different O₂/C in the reduced agent are illustrated in Figure 10. Observations reveal that T1 remains approximately constant at around 900 °C for various experimental conditions in this series, indicating stable operation of the activation unit. As the O₂/C in the reduced agent increases, the intensity of the combustion reaction in the reduction unit increases, resulting in a gradual increase in both T9 and T10. It can be observed that, compared to T9, the change in T10 is more pronounced with O₂/C in the reduced agent increasing. This suggests that as O₂/C in the reduced agent increases, the zone where the combustion reaction occurs expands, no longer confined to the top zone of the reduction unit. The combustion reaction is constrained by the combination of mixing effects, mass transfer effects and reaction rates.

The time taken for the completion of the combustion reaction is significantly influenced by the O_2/C . As the O_2/C increases, more oxygen that has not reacted departs from the top zone, and combustion initiates in the middle zone. Consequently, the combustion reaction extends to the middle zone. On the other hand, with the increase in O_2/C , the amount of the reduced agent also increases. This results in the increase in flow velocity of high-temperature gases in the reduction unit and contributes to a more uniform temperature distribution in the reduction unit.

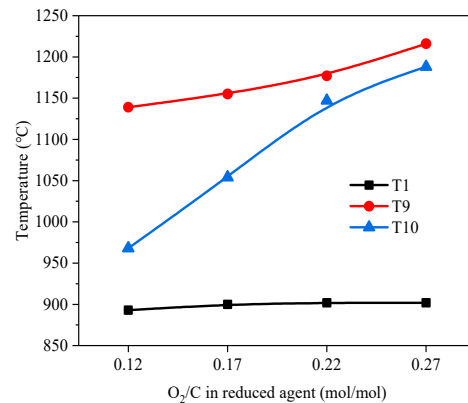


Figure 10. The temperature profiles under different O_2/C in the reduced agent.

Comparing the impact of CO_2 concentration in the reduced agent on the temperature profiles in the reduction unit in Figure 6, it can be inferred that both O_2/C and CO_2 concentration affect the temperature profiles by influencing the region where the combustion reaction occurs. But their mechanisms differ. When O_2/CO_2 is used as the reduced agent, the CO_2 concentration primarily affects the combustion reaction rates, prompting the movement of the zone where the combustion reaction occurs. On the other hand, O_2/C affects the time required for the completion of the combustion reaction, determining the size of the zone where the combustion reaction occurs. Accordingly, the impact of CO_2 concentration on T9 is more significant, while the impact of O_2/C is more pronounced on T10.

The composition of the activation unit gas and component net yields in the activation unit are illustrated in Figure 11. Similar to Figure 7, the concentrations of CO and CO_2 in the activation unit gas are close, but there is a significant difference in their yields. This is also due to the inclusion of CO_2 from the active agent in the activation unit gas. In comparison to the experimental conditions in Section 3.1, in this series of conditions, the oxygen concentration and O_2/C in the active agent are higher, resulting in a higher T1 (around 900 °C in this series compared to around 800 °C in Section 3.1). The higher temperature enhances the Boudouard reaction, leading to a higher CO production.

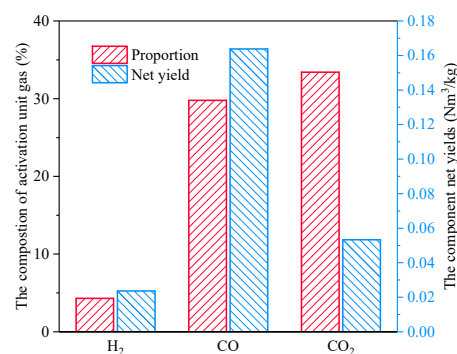


Figure 11. The situation of the activation unit gas under different O_2/C in the reduced agent.

The situation of reactions in the reduction unit under different O_2/C in the reduced agent is illustrated in Figure 12. The intensities of three main reactions increase with the rise

in O_2/C in the reduced agent. On the one hand, the intensity of the combustion reaction enhances with the increase in O_2/C . And on the other hand, the intensified combustion reaction elevates the temperature, leading to an increase in the intensities of the Boudouard and the steam char gasification reactions. When O_2/C in the reduced agent increases from 0.12 to 0.22, the increase in the intensity of the Boudouard reaction is greater than that of the combustion reaction. The proportion of the Boudouard reaction increases (from 49.1% to 51.9%), while simultaneously, the proportion of the combustion reaction decreases (from 45.4% to 41.9%). One possible reason is that the intensity of the combustion reaction is approximately linearly related to O_2/C and independent of temperature, while the relationship between the Boudouard reaction and temperature approximately follows Arrhenius form. This results in a more significant change in the Boudouard reaction when CO_2 generation linearly increases, accompanied by a notable rise in temperature. Correspondingly, from Figure 12, it can be observed that the slope of the combustion reaction curve is approximately constant. However, the slope of the Boudouard reaction curve is generally higher than that of the combustion reaction when O_2/C is between 0.17 and 0.22. With further increase in O_2/C , the slope of the Boudouard reaction curve begins to decline, even though temperature is increasing. This suggests that the Boudouard reaction is inhibited, and this effect will be explained later.

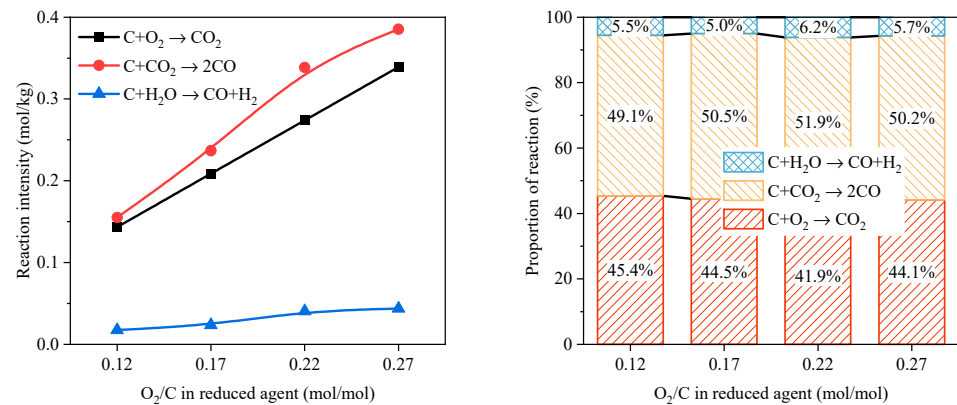


Figure 12. The situation of reactions under different O_2/C in the reduced agent.

The composition of the reduction unit gas and component yields in the reduction unit under different O_2/C in the reduced agent are depicted in Figure 13. As the O_2/C in the reduced agent increases, the concentration of CO in the reduction unit gas first increases and then decreases. The trend for CO_2 is the opposite. The content of H_2 remains relatively stable and essentially unchanged. CO is generated not only by the Boudouard reaction but also by the combustion reaction. Therefore, CO yield in the reduction unit gradually decreases as the O_2/C in the reduced agent decreases. With the increase in O_2/C , the generation of CO_2 intensifies. This is because one of the products of the combustion reaction is CO_2 , and CO can also be oxidized to CO_2 by O_2 . At the same time, as the temperature increases, the Boudouard reaction is enhanced, leading to an increase in the reduction of CO_2 . When O_2/C in the reduced agent is increased from 0.12 to 0.22, the operating temperature increases significantly, enhancing the Boudouard reaction and gradually increasing the reduction of CO_2 . When the O_2/C of the reduced agent increases from 0.22 to 0.27, the CO concentration approaches its upper limit (55%), and the Boudouard reaction is inhibited. At the same time, the increase in temperature is not significant. The enhanced combustion reaction leads to a more pronounced generation of CO_2 , and the reduction of CO_2 begins to decrease. When the O_2/C in the reduced agent is 0.22, the maximum CO_2 net reduction is achieved, reaching $0.065 \text{ Nm}^3/\text{kg}$.

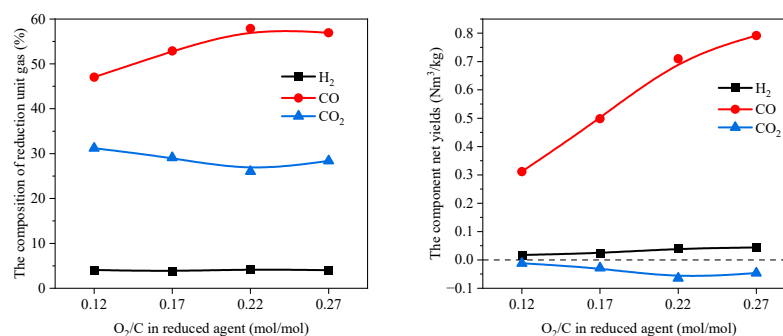


Figure 13. The situation of the reduction unit gas under different O₂/C in the reduced agent.

3.3. Effect of Different Coal Gasification Chars

The physicochemical properties vary among different carbon-based materials, affecting their ability to reduce CO₂. In this series of experimental conditions, YHGC and CPGC are chosen as the materials. The reduction capabilities and performances of different coal gasification chars in the activation reduction process for CO₂ are investigated. The experimental conditions for this series are presented in Table 5.

Table 5. Experimental conditions for different coal gasification chars in the reduced agent.

No.	Material	Feed Rate (kg/h)	The Active Agent		The Reduced Agent	
			Composition	O ₂ /C (Mol/Mol)	Composition	O ₂ /C (Mol/Mol)
6	YHGC	23	O ₂ /CO ₂ (50%/50%)	0.11	O ₂ /CO ₂ (50%/50%)	0.12
10	CPGC	32	O ₂ /CO ₂ (31%/69%)	0.15	O ₂ /CO ₂ (60%/40%)	0.10

During the experimental process, the composition of the active agent was adjusted to maintain the temperature of the activation unit approximately constant. By adjusting the CO₂ concentration and O₂/C in the reduced agent, it was ensured that T9 under both experimental conditions were approximately consistent.

The temperature distribution is illustrated in Figure 14. It can be observed that the temperatures of the two operating conditions are approximately consistent. T1 is around 900 °C, and T9 is around 1150 °C. T10 exhibits a significant difference. T9 and T10 are closer, when CPGC is used as the material. The active agent O₂/C in experimental condition No. 10 is higher, resulting in a larger flow of the activation unit gas. This leads to a higher gas flow rate in the DR, resulting in a more uniform distribution of heat. Additionally, the differences between different raw materials are also factors influencing the temperature.

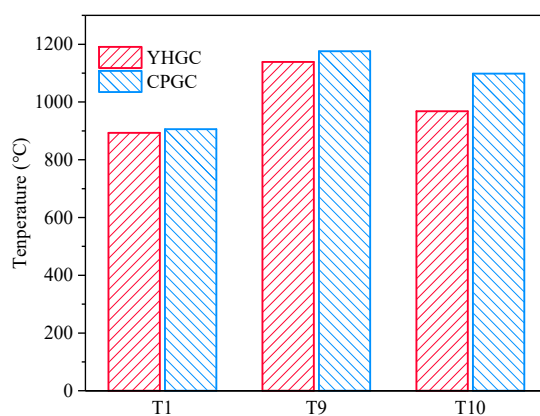


Figure 14. The temperature profiles under different coal gasification chars.

The figures of the different chars are shown in Figure 15. In terms of their actual appearance, all the four kinds of chars appear as black particles with no significant differences. However, the particles of YHGC and CPGC tend to cluster together. On the other hand, the distribution of particles in activated char (YHGC-char and CPGC-char) tends to be more dispersed. In the actual figures, the state presented by activated char appears more diffuse.

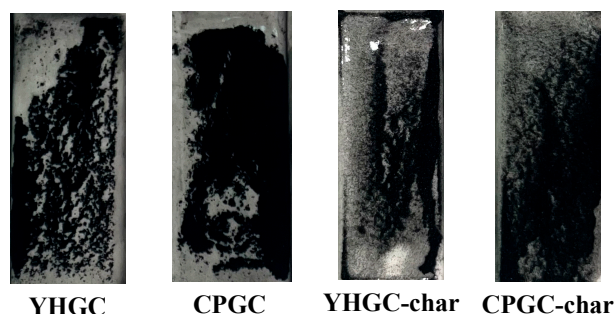


Figure 15. The figures of different chars.

The SEM micrographs of the different chars are shown in Figure 16. YHGC and CPGC are gasification chars, hence there are some noticeably larger pores on their surfaces. In comparison to YHGC, the metallic aggregates of CPGC not only distribute across the surface but also appear abundantly in the pores. It can be observed that, compared to YHGC and CPGC, the surfaces of YHGC-char and CPGC-char are rougher, with many smaller pores present. These result from the participation of solid-phase carbon in combustion and the Boudouard reaction during the activation process, leading to the consumption of solid carbon on the surface.

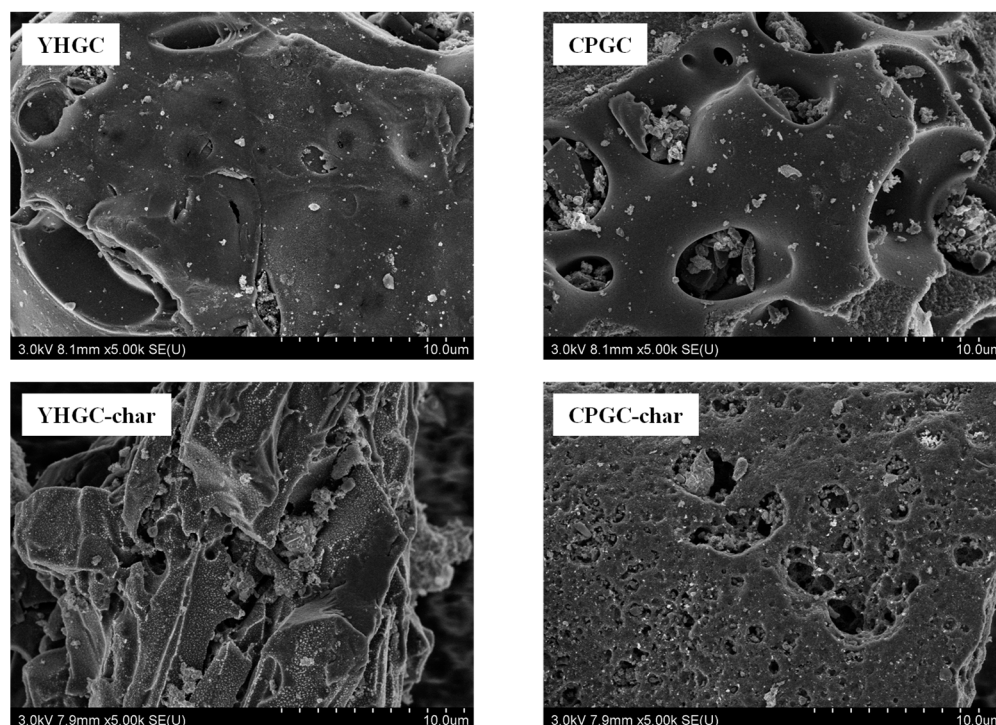


Figure 16. SEM micrographs of different chars.

The pore structures of the different chars are shown in Table 6. Compared to CPGC, the specific surface area and pore volume of YHGC are larger. This means that YHGC can provide a more extensive area for the Boudouard reaction to take place. The average pore diameters of YHGC and CPGC are similar, indicating that their pore structures are

approximately alike. The difference in specific surface area and pore volume arises from variations in the quantity of pores. YHGC-char and CPGC-char refer to the activated chars formed from YHGC and CPGC, respectively. Due to differences between YHGC and CPGC, the specific surface area of the two activated chars shows significant variation, but this difference diminishes. In comparison to the raw materials, both the pore volume and average pore diameter of the two activated chars have decreased to varying degrees. The activation process alters the pore structure of the raw materials, with larger pores being consumed and smaller pores developing.

Table 6. The pore structures of different chars.

	Specific Surface Area (m ² /g)	Pore Volume (cm ³ /g)	Average Pore Diameter (Å)
YHGC	561.2566	0.659410	52.9117
YHGC-char	555.6712	0.530141	50.5930
CPGC	180.9190	0.251470	55.5980
CPGC-char	238.3206	0.144802	38.2710

The Raman original spectra of different chars are shown in Figure 17, and the results are shown in Figure 18. Comparison between the coal gasification chars (YHGC and CPGC) and their activated chars (YHGC-char and CPGC-char) indicates that the ratios of I_G/I_{all} and I_{D3+D4}/I_G are essentially consistent. YHGC and CPGC are derived from the CFB gasification plant, having undergone a complete gasification process, thus having stable carbon structures. In the activation unit, the Boudouard reaction consumes carbon structures while increasing active sites. However, the high activated temperature partially promotes carbon microcrystal agglomeration, leading to active sites consumption. In contrast to I_G/I_{all} and I_{D3+D4}/I_G , the difference in I_{D1}/I_G is relatively pronounced, suggesting the possibility of the Boudouard reaction occurring in the aromatic layers, promoting in-plane defect generation and expansion, where the high temperature exerts less significant inhibition on these defects. This could be attributed to the carbon microcrystal agglomeration primarily occurring between different microcrystals, thereby covering active sites located at the edge while having little effect on the in-plane defects. Additionally, it can be observed that YHGC-char has a lower degree of graphitization, a higher content of disorder carbon, and a higher quantity of in-plane defects in the aromatic layers. Raman results indicate that YHGC-char exhibits higher carbon structural reactivity. However, in comparison to the differences in pore structure, the differences in carbon structure are not pronounced.

The $R_{0.5}$ obtained from TGA of the different chars is depicted in Figure 19. The $R_{0.5}$ of YHGC and its activated char (YHGC-char) are essentially similar, with the $R_{0.5}$ of YHGC-char being only 1.31% higher than that of YHGC. This is mainly attributed to the similar pore structure and carbon structure between YHGC and YHGC-char. Due to the relatively higher content of in-plane defects in YHGC-char, the reaction reactivity of YHGC-char is slightly higher, despite YHGC-char having a slightly lower specific surface area compared to YHGC. Following activation, the $R_{0.5}$ of CPGC-char is 11.45% higher than that of CPGC. This difference is more pronounced than the corresponding difference for YHGC. As observed from Table 6, the specific surface area of CPGC-char is significantly higher than CPGC, which is distinct from YHGC. Both YHGC and CPGC exhibit stable carbon structures, with minimal differences before and after the activation process, suggesting that the carbon structures have limited impact on reactivity. The variation in specific surface area induced by the activation process is identified as the key factor influencing the activated effects of YHGC and CPGC. The larger specific surface area of YHGC corresponds to a more mature pore structure that is less susceptible to change, whereas the pore structure of CPGC is more easily altered by the activation process.

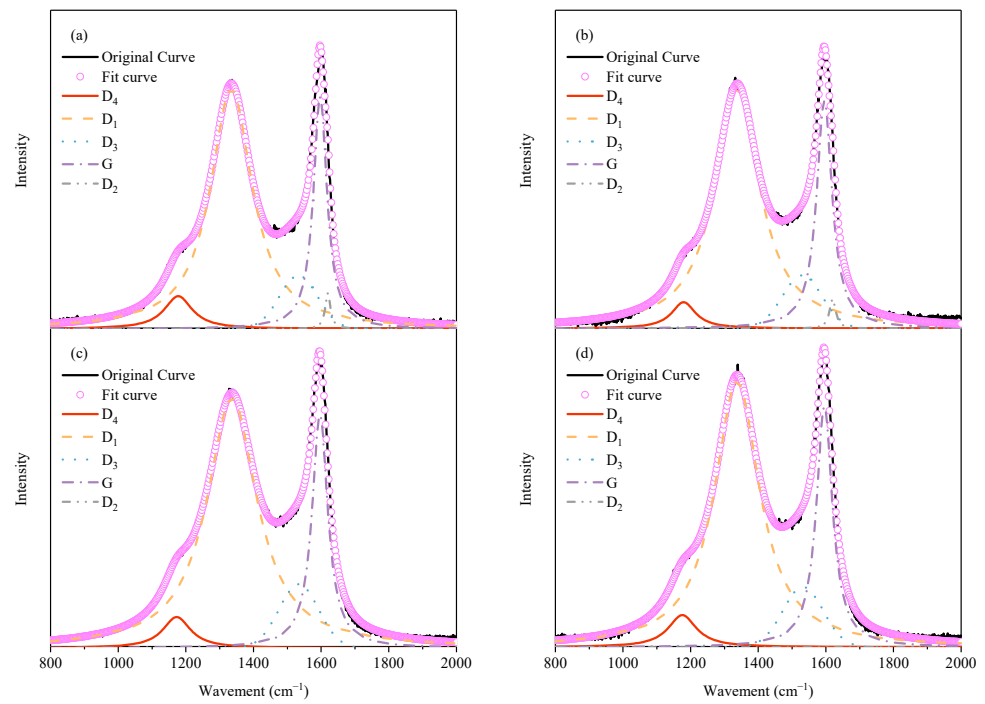


Figure 17. Raman original spectra of YHGC (a), CPGC (b), YHGC-char (c) and CPGC-char (d).

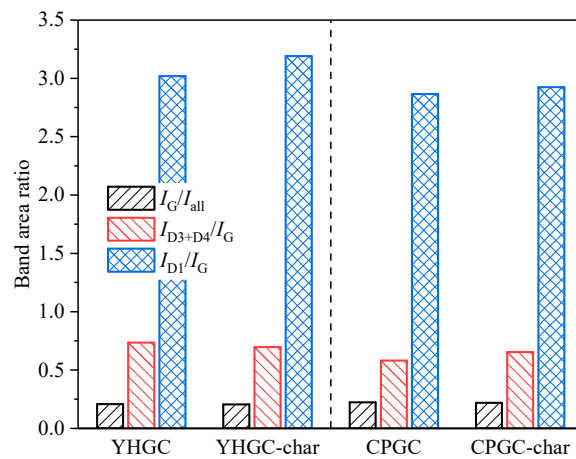


Figure 18. The Raman spectra results of different chars.

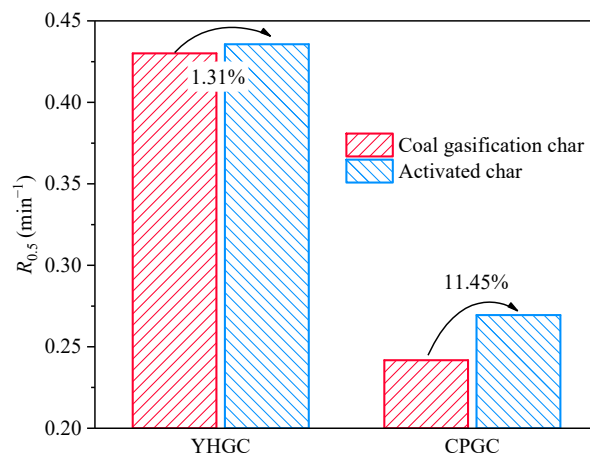


Figure 19. The $R_{0.5}$ obtained from TGA of different chars.

Furthermore, there are notable differences between YHGC and CPGC, and this difference is inherited by their activated chars. These differences primarily stem from variations in specific surface area rather than carbon structure (Figure 18 shows no significant differences in carbon structure among the four chars). This is consistent with the previously mentioned importance of specific surface area. This suggests that the activation process can, to some extent, mitigate differences between raw materials. However, in the range of activation conditions utilized in this study, the mitigating effect of the activation process on differences is limited. This may be attributed to the fine particle size of YHGC and CPGC, making it difficult for the cyclone separator of the activation unit to achieve more effective separation. Improved separation efficiency could prolong the activated time of char, thereby facilitating further development of pore structure by the Boudouard reaction. The selection range of the active agent O_2/C and active temperature also influence activation effectiveness.

The composition of the activation unit gas and component net yields in the activation units for different raw materials is shown in Figure 20. Compared to CPGC, when YHGC is used as the raw material, the activation unit gas has a higher CO content, while the CO_2 content is only half of that when CPGC is used as the raw material. This is partly because when CPGC is used as the raw material, O_2/C and CO_2 concentrations in the active agent are higher. The higher O_2/C enhances combustion reactions, leading to more CO_2 production. Additionally, the higher CO_2 concentration results in more CO_2 being introduced into the activation unit and retained in the activation unit gas. On the other hand, YHGC has a larger specific surface area, and the reactivity of YHGC is higher. The yields of components in the activation unit also support this point. At similar temperatures, when YHGC is used as the raw material, the yield of CO_2 is half that of CPGC. This indicates that the Boudouard reaction is more pronounced when YHGC is used as the raw material.

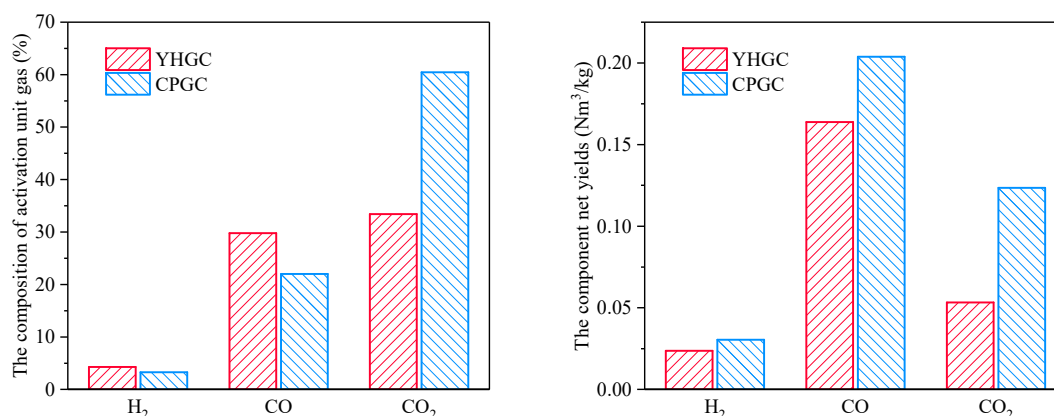


Figure 20. The situation of the activation unit gas under different coal gasification chars.

The situation of reactions in the reduction unit under different chars is illustrated in Figure 21. Due to the higher O_2/C (0.12, shown in Table 5) of YHGC as the raw materials, the combustion reaction intensity in the reduction unit is higher. As shown in Figure 19, YHGC-char exhibits higher reactivity, resulting in a stronger Boudouard reaction intensity at a similar reduction temperature. This suggests that the reactivity of activated char significantly influences the strength of the Boudouard reaction in the reduction unit. The reactivity of activated char is directly related to the intensity of the Boudouard reaction in the reduction unit. The content of hydrogen-containing components in the system is very small, so the difference in the intensity of the steam char gasification reaction (R6) between these two experiment conditions is not obvious. The situation in reaction proportions further highlights the differences in the Boudouard reaction intensity. Although YHGC as a raw material has the higher combustion reaction intensity in the reduction unit, its ratio is still lower than CPGC (45.4% vs. 49.2%). The difference in the Boudouard reaction

intensity resulting from the disparity in reactivity between YHGC-char and CPGC-char is more pronounced compared to the difference in combustion reaction intensity. The direct relationship of activated char reactivity and the Boudouard reaction intensity illustrates that the activation process enhances the reactivity of char towards CO₂ reduction. According to the relationship between the reactivity of activated char and the Boudouard reaction, the activation process can improve the reactivity of activated char, which is conducive to the reduction of CO₂.

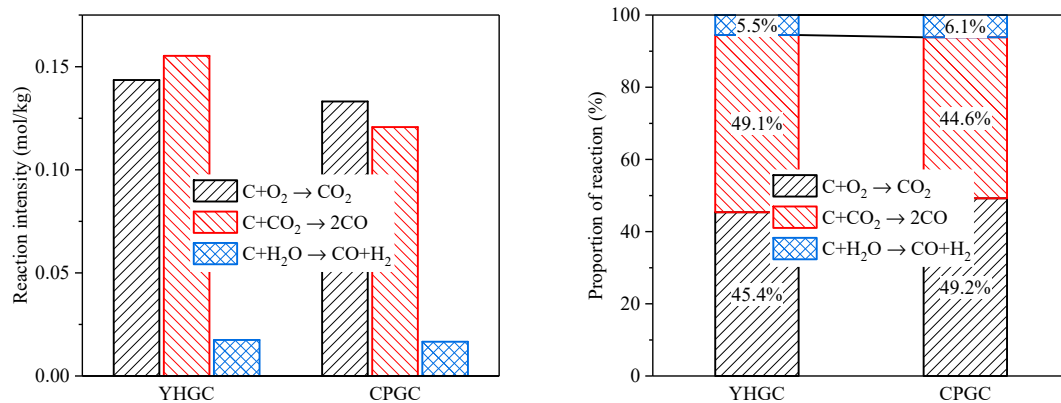


Figure 21. The situation of reactions under different coal gasification chars.

The composition of the reduction unit gas and component yields in the reduction unit for the different raw materials is shown in Figure 22. When YHGC is used as the raw materials, the CO content in the reduction unit gas is significantly higher, while the CO₂ content is lower. Part of the reason is that more CO₂ is introduced into the system when CPGC is used as the raw material. The components' net yields in the reduction unit are also one of the reasons. It can be observed that when YHGC is used as the raw material, there is a greater net generation of CO, and the net reduction of CO₂ is achieved (the negative of the net yield) in the reduction unit. This can be attributed to differences in reaction intensities in the reduction unit. The higher reactivity of YHGC-char results in stronger Boudouard reactions at the same temperature, lower CO₂ concentration, and lower carbon concentration (due to the lower feed rate of YHGC), ultimately leading to an increased net reduction of CO₂. Compared with CPGC, YHGC is more suitable for CO₂ reduction because of its high reactivity. And this high reactivity comes from the high specific surface area. Moreover, this also shows that the impact of activated char reactivity is more significant compared to CO₂ concentration and carbon concentrations. From the perspective of reactivity, CPGC-char is more suitable for CO₂ reduction than CPGC. The presence of activation processes significantly enhances the reactivity of CPGC, thereby making the difference between these two activated chars less than that of these two raw materials. The effect of CO₂ reduction is determined by the reactivity of activated char.

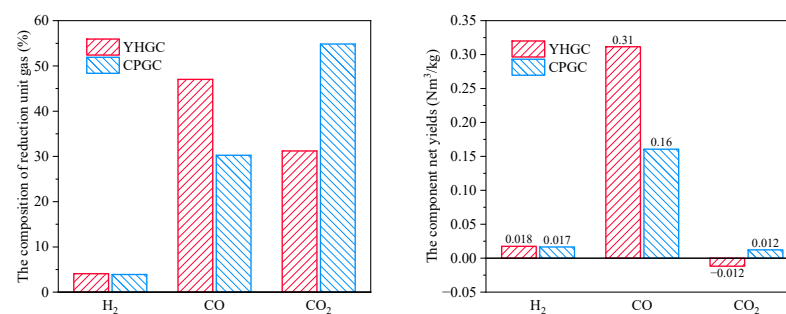


Figure 22. The situation of the reduction unit gas under different coal gasification chars.

4. Conclusions

These experiments aimed to study the reduction of CO₂ using coal gasification char through activated-reduction technology on an activated-reduction bench-scale self-sustained platform. The impact of CO₂ concentration and O₂/C in the reduced agent on CO₂ reduction was investigated. The effects of two typical coal gasification chars on CO₂ reduction through activated-reduction technology were also studied. The main results are summarized as follows:

(1) The influence mechanisms of CO₂ concentration and O₂/C in the reduced agent on temperature in the reduction unit are different. The CO₂ concentration affects the temperature profiles mainly by promoting the shift of the combustion reaction zone. O₂/C mainly affects the size of the combustion reaction zone.

(2) Both CO concentration and temperature affect CO₂ reduction by influencing the intensity of the Boudouard reaction. Near the upper limit of CO concentration, CO concentration significantly inhibited CO₂ reduction. At 1200 °C, the upper limit is about 55%. At a distance from CO concentration, temperature significantly affects CO₂ reduction.

(3) When the reduced agent O₂/C is 0.18, CO₂ concentration of 60% is the best parameter for CO₂ reduction. The corresponding net CO₂ reduction is 0.021 Nm³/kg. When CO₂ concentration in the reduced agent is 50%, O₂/C of 0.22 is the best parameter for CO₂ reduction, corresponding to the net CO₂ reduction of 0.065 Nm³/kg.

(4) The activation process has different effects on the reactivity of different coal gasification chars and can narrow the differences between raw materials. For YHGC-char, R0.5 is 1.31% higher than that of YHGC, while for CPGC, the difference is 11.45%. In addition, YHGC has a higher specific surface area, so its reactivity is higher, and it is more suitable for CO₂ reduction. The activation process improves the reactivity of coal gasification chars and is beneficial to CO₂ reduction in the reduction unit.

Author Contributions: Investigation and Writing—original draft, S.Z.; Conceptualization and Writing—review and editing, C.L.; Conceptualization and Project administration, Z.Z.; Investigation, R.C. All authors have read and agreed to the published version of the manuscript.

Funding: Supported by the Strategic Priority Research Program of the Chinese Academy of Sciences, Grant No. XDA 29030100.

Data Availability Statement: The raw data supporting the conclusions of this article will be made available by the authors on request.

Conflicts of Interest: The authors declare no conflicts of interest.

Abbreviations

A _{ad}	The content of ash on the air-dry basis
CFB	Circulating fluidized bed
CPGC	Chiping gasification char
CPGC-char	Activated char of CPGC
DR	Downdraft reactor
FC _{ad}	The content of fixed carbon on the air-dry basis
M _{ad}	The content of moisture on the air-dry basis
Q _{net,ad}	The net calorific value on the air-dry basis
TGA	Thermogravimetric analysis
V _{ad}	The content of volatiles on the air-dry basis
WGSR	Water gas shift reaction
YHGC	Yihua gasification char
YHGC-char	Activated char of YHGC

References

1. Zhi, K.; Li, Z.; Wang, B.; Klemeš, J.J.; Guo, L. A review of CO₂ utilization and emissions reduction: From the perspective of the chemical engineering. *Process Saf. Environ. Prot.* **2023**, *172*, 681–699. [\[CrossRef\]](#)
2. Theofanidis, S.A.; Antzaras, A.N.; Lemonidou, A.A. CO₂ as a building block: From capture to utilization. *Curr. Opin. Chem. Eng.* **2023**, *39*, 100902. [\[CrossRef\]](#)
3. Chan, Y.H.; Syed Abdul Rahman, S.N.F.; Lahuri, H.M.; Khalid, A. Recent progress on CO-rich syngas production via CO₂ gasification of various wastes: A critical review on efficiency, challenges and outlook. *Environ. Pollut.* **2021**, *278*, 116843. [\[CrossRef\]](#) [\[PubMed\]](#)
4. Sabri, M.A.; Al Jitan, S.; Bahamon, D.; Vega, L.F.; Palmisano, G. Current and future perspectives on catalytic-based integrated carbon capture and utilization. *Sci. Total Environ.* **2021**, *790*, 148081. [\[CrossRef\]](#) [\[PubMed\]](#)
5. Lu, W.; Cao, Q.; Xu, B.; Adidharma, H.; Gasem, K.; Argyle, M.; Zhang, F.; Zhang, Y.; Fan, M. A new approach of reduction of carbon dioxide emission and optimal use of carbon and hydrogen content for the desired syngas production from coal. *J. Clean. Prod.* **2020**, *265*, 121786. [\[CrossRef\]](#)
6. Antolini, D.; Ail, S.S.; Patuzzi, F.; Grigiente, M.; Baratieri, M. Experimental investigations of air-CO₂ biomass gasification in reversed downdraft gasifier. *Fuel* **2019**, *253*, 1473–1481. [\[CrossRef\]](#)
7. Lahijani, P.; Zainal, Z.A.; Mohammadi, M.; Mohamed, A.R. Conversion of the greenhouse gas CO₂ to the fuel gas CO via the Boudouard reaction: A review. *Renew. Sustain. Energy Rev.* **2015**, *41*, 615–632. [\[CrossRef\]](#)
8. Qinggang, L.; Zhen, C. Highly efficient and clean utilization of fossil energy under carbon peak and neutrality targets. *Bull. Chin. Acad. Sci.* **2022**, *37*, 541–548.
9. Hunt, J.; Ferrari, A.; Lita, A.; Crosswhite, M.; Ashley, B.; Stiegman, A.E. Microwave-Specific Enhancement of the Carbon–Carbon Dioxide (Boudouard) Reaction. *J. Phys. Chem. C* **2013**, *117*, 26871–26880. [\[CrossRef\]](#)
10. Shurtz, R.C.; Fletcher, T.H. Coal Char-CO₂ Gasification Measurements and Modeling in a Pressurized Flat-Flame Burner. *Energy Fuels* **2013**, *27*, 3022–3038. [\[CrossRef\]](#)
11. Vamvuka, D.; Karouki, E.; Sfakiotakis, S. Gasification of waste biomass chars by carbon dioxide via thermogravimetry. Part I: Effect of mineral matter. *Fuel* **2011**, *90*, 1120–1127. [\[CrossRef\]](#)
12. Duman, G.; Uddin, M.A.; Yanik, J. The effect of char properties on gasification reactivity. *Fuel Process. Technol.* **2014**, *118*, 75–81. [\[CrossRef\]](#)
13. Tong, W.; Liu, Q.; Yang, C.; Cai, Z.; Wu, H.; Ren, S. Effect of pore structure on CO₂ gasification reactivity of biomass chars under high-temperature pyrolysis. *J. Energy Inst.* **2020**, *93*, 962–976. [\[CrossRef\]](#)
14. Zhang, X.; Zhu, S.; Zhu, J.; Liu, Y.; Zhang, J.; Hui, J.; Ding, H.; Cao, X.; Lyu, Q. Preheating and combustion characteristics of anthracite under O₂/N₂, O₂/CO₂ and O₂/CO₂/H₂O atmospheres. *Energy* **2023**, *274*, 127419. [\[CrossRef\]](#)
15. Su, K.; Ouyang, Z.; Ding, H.; Wang, W.; Zhang, J.; Wang, H.; Zhu, S. Experimental investigation on effect of external circulation system on preheating characteristics of pulverized coal. *Energy* **2023**, *278*, 127781. [\[CrossRef\]](#)
16. Jiang, D.; Song, W.; Wang, X.; Zhu, Z. Physicochemical properties of bottom ash obtained from an industrial CFB gasifier. *J. Energy Inst.* **2021**, *95*, 1–7. [\[CrossRef\]](#)
17. Guizani, C.; Jeguirim, M.; Valin, S.; Limousy, L.; Salvador, S. Biomass Chars: The Effects of Pyrolysis Conditions on Their Morphology, Structure, Chemical Properties and Reactivity. *Energies* **2017**, *10*, 796. [\[CrossRef\]](#)
18. Zhang, X.-s.; Song, X.-d.; Su, W.-g.; Wei, J.-t.; Bai, Y.-h.; Yu, G.-s. In-situ study on gasification reaction characteristics of Ningdong coal chars with CO₂. *J. Fuel Chem. Technol.* **2019**, *47*, 385–392. [\[CrossRef\]](#)
19. Liu, Y.; Liu, J.; Lyu, Q.; Zhu, J.; Pan, F. Microstructure analysis of fluidized preheating pulverized coal under O₂/CO₂ atmospheres. *Fuel* **2021**, *292*, 120386. [\[CrossRef\]](#)
20. Zhang, Y.; Zhu, J.; Lyu, Q.; Liu, J.; Pan, F. Coke generation and conversion behavior of pulverized coal combustion. *J. Energy Inst.* **2020**, *93*, 2096–2107. [\[CrossRef\]](#)
21. Liang, C.; Lyu, Q.; Na, Y.; Wang, X. Gasification of preheated coal: Experiment and thermodynamic equilibrium calculation. *J. Energy Inst.* **2019**, *92*, 1005–1013. [\[CrossRef\]](#)
22. Ding, H.; Ouyang, Z.; Shi, Y.; Chen, R.; Zhang, Z.; Zhu, S.; Lyu, Q. Effects of the T-abrupt exit configuration of riser on fuel properties, combustion characteristics and NO_x emissions with coal self-preheating technology. *Fuel* **2023**, *337*, 126860. [\[CrossRef\]](#)
23. Mahinpey, N.; Gomez, A. Review of gasification fundamentals and new findings: Reactors, feedstock, and kinetic studies. *Chem. Eng. Sci.* **2016**, *148*, 14–31. [\[CrossRef\]](#)
24. Wang, Z.; Burra, K.G.; Li, X.; Zhang, M.; He, X.; Lei, T.; Gupta, A.K. CO₂-assisted gasification of polyethylene terephthalate with focus on syngas evolution and solid yield. *Appl. Energy* **2020**, *276*, 115508. [\[CrossRef\]](#)
25. Singh, P.; Déparrois, N.; Burra, K.G.; Bhattacharya, S.; Gupta, A.K. Energy recovery from cross-linked polyethylene wastes using pyrolysis and CO₂ assisted gasification. *Appl. Energy* **2019**, *254*, 113722. [\[CrossRef\]](#)
26. Wang, B.; Xu, F.; Wang, X.; Li, J.; Song, Y.; Qiao, Y.; Tian, Y. Comparative study on pyrolysis and gasification within CO₂ atmosphere of typical forestry biomass in Northeast Asia: Thermal behavior and kinetic analysis. *Fuel* **2022**, *324*, 124540. [\[CrossRef\]](#)
27. Liu, T.-f.; Fang, Y.-t.; Wang, Y. An experimental investigation into the gasification reactivity of chars prepared at high temperatures. *Fuel* **2008**, *87*, 460–466. [\[CrossRef\]](#)

28. Jing, X.; Wang, Z.; Yu, Z.; Zhang, Q.; Li, C.; Fang, Y. Experimental and Kinetic Investigations of CO₂ Gasification of Fine Chars Separated from a Pilot-Scale Fluidized-Bed Gasifier. *Energy Fuels* **2013**, *27*, 2422–2430. [[CrossRef](#)]
29. Xie, Y.; Yang, H.; Zeng, K.; Zhu, Y.; Hu, J.; Mao, Q.; Liu, Q.; Chen, H. Study on CO₂ gasification of biochar in molten salts: Reactivity and structure evolution. *Fuel* **2019**, *254*, 115614. [[CrossRef](#)]
30. Liang, C.; Zhang, H.; Zhu, Z.; Na, Y.; Lu, Q. CO₂-O₂ gasification of a bituminous coal in circulating fluidized bed. *Fuel* **2017**, *200*, 81–88. [[CrossRef](#)]
31. Feroso, J.; Stevanov, C.; Moghtaderi, B.; Arias, B.; Pevida, C.; Plaza, M.G.; Rubiera, F.; Pis, J.J. High-pressure gasification reactivity of biomass chars produced at different temperatures. *J. Anal. Appl. Pyrolysis* **2009**, *85*, 287–293. [[CrossRef](#)]
32. Malekshahian, M.; Hill, J.M. Kinetic Analysis of CO₂ Gasification of Petroleum Coke at High Pressures. *Energy Fuels* **2011**, *25*, 4043–4048. [[CrossRef](#)]
33. Wall, T.F.; Liu, G.-s.; Wu, H.-w.; Roberts, D.G.; Benfell, K.E.; Gupta, S.; Lucas, J.A.; Harris, D.J. The effects of pressure on coal reactions during pulverised coal combustion and gasification. *Prog. Energy Combust. Sci.* **2002**, *28*, 405–433. [[CrossRef](#)]
34. Hüttinger, K.J.; Nill, J.S. A method for the determination of active sites and true activation energies in carbon gasification: (II) Experimental results. *Carbon* **1990**, *28*, 457–465. [[CrossRef](#)]
35. Ahmed, I.I.; Gupta, A.K. Kinetics of woodchips char gasification with steam and carbon dioxide. *Appl. Energy* **2011**, *88*, 1613–1619. [[CrossRef](#)]
36. Irfan, M.F.; Usman, M.R.; Kusakabe, K. Coal gasification in CO₂ atmosphere and its kinetics since 1948: A brief review. *Energy* **2011**, *36*, 12–40. [[CrossRef](#)]
37. Kajitani, S.; Hara, S.; Matsuda, H. Gasification rate analysis of coal char with a pressurized drop tube furnace. *Fuel* **2002**, *81*, 539–546. [[CrossRef](#)]
38. Zhu, L.; Wang, Y.; Zhang, Z.; Li, J.; Yu, G. Effects of H₂ and CO on Char-Gasification Reactivity at High Temperatures. *Energy Fuels* **2020**, *34*, 720–727. [[CrossRef](#)]
39. Zhang, S.; Liang, C.; Wang, X.; Zhu, Z. Experimental study and equilibrium analysis on thermal reduction of CO₂ by CFB gasification. *J. Energy Inst.* **2024**, 101623. [[CrossRef](#)]
40. Yang, Q.; Qi, X.; Lyu, Q.; Zhu, Z. Physicochemical Properties of Coal Gasification Fly Ash from Circulating Fluidized Bed Gasifier. *J. Therm. Sci.* **2023**, *32*, 1710–1720. [[CrossRef](#)]
41. Liu, D.; Wang, W.; Tu, Y.; Ren, G.; Yan, S.; Liu, H.; He, H. Flotation specificity of coal gasification fine slag based on release analysis. *J. Clean. Prod.* **2022**, *363*, 132426. [[CrossRef](#)]
42. Kou, M.; Zuo, H.; Ning, X.; Wang, G.; Hong, Z.; Xu, H.; Wu, S. Thermogravimetric study on gasification kinetics of hydrolysis char derived from low rank coal. *Energy* **2019**, *188*, 116030. [[CrossRef](#)]
43. Chen, C.; Tang, Y.; Guo, X. Comparison of structural characteristics of high-organic-sulfur and low-organic-sulfur coal of various ranks based on FTIR and Raman spectroscopy. *Fuel* **2022**, *310*, 122362. [[CrossRef](#)]
44. Dresselhaus, M.S.; Dresselhaus, G. Intercalation compounds of graphite. *Adv. Phys.* **1981**, *30*, 139–326. [[CrossRef](#)]
45. Su, K.; Ding, H.; Ouyang, Z.; Zhang, J.; Zhu, S. Experimental study on effects of multistage reactant and air jet velocities on self-preheating characteristics and NO_x emission of burning pulverized coal. *Fuel* **2022**, *325*, 124879. [[CrossRef](#)]
46. Guedes, A.; Valentim, B.; Prieto, A.C.; Noronha, F. Raman spectroscopy of coal macerals and fluidized bed char morphotypes. *Fuel* **2012**, *97*, 443–449. [[CrossRef](#)]
47. Jayaraman, K.; Gokalp, I. Effect of char generation method on steam, CO₂ and blended mixture gasification of high ash Turkish coals. *Fuel* **2015**, *153*, 320–327. [[CrossRef](#)]
48. Ma, C.; Zhao, Y.; Lang, T.; Zou, C.; Zhao, J.; Miao, Z. Pyrolysis characteristics of low-rank coal in a low-nitrogen pyrolysis atmosphere and properties of the prepared chars. *Energy* **2023**, *277*, 127524. [[CrossRef](#)]
49. Frederick, W.J.; Wag, K.J.; Hupa, M.M. Rate and mechanism of black liquor char gasification with carbon dioxide at elevated pressures. *Ind. Eng. Chem. Res.* **1993**, *32*, 1747–1753. [[CrossRef](#)]
50. Mitsuoka, K.; Hayashi, S.; Amano, H.; Kayahara, K.; Sasaoaka, E.; Uddin, M.A. Gasification of woody biomass char with CO₂: The catalytic effects of K and Ca species on char gasification reactivity. *Fuel Process. Technol.* **2011**, *92*, 26–31. [[CrossRef](#)]

Disclaimer/Publisher’s Note: The statements, opinions and data contained in all publications are solely those of the individual author(s) and contributor(s) and not of MDPI and/or the editor(s). MDPI and/or the editor(s) disclaim responsibility for any injury to people or property resulting from any ideas, methods, instructions or products referred to in the content.